

Magnetic and magnetocaloric effect of $Er_{20}Ho_{20}Dy_{20}Cu_{20}Ni_{20}$ high-entropy metallic glass

Shi-Lin Yu, Lu Tian, Jun-Feng Wang, Xin-Guo Zhao, Da Li, Zhao-Jun Mo, and Bing Li

Citation: Chin. Phys. B, 2024, 33 (**5**): 057502. DOI: 10.1088/1674-1056/ad1a94
Journal homepage: http://cpb.iphy.ac.cn; http://iopscience.iop.org/cpb

What follows is a list of articles you may be interested in

Analytical solutions to the precession relaxation of magnetization with uniaxial anisotropy

Ze-Nan Zhang(张泽南), Zhen-Lin Jia(贾镇林), and De-Sheng Xue(薛德胜)
Chin. Phys. B, 2024, 33 (**4**): 047502. DOI: 10.1088/1674-1056/ad08a3

Enhanced resonance frequency in Co_2FeAl thin film with different thicknesses grown on flexible graphene substrate

Cai Zhou(周偲), Shaokang Yuan(袁少康), Dengyu Zhu(朱登玉), Yuming Bai(白宇明), Tao Wang(王韬), Fufu Liu(刘福福), Lulu Pan(潘禄禄), Cunfang Feng(冯存芳), Bohan Zhang(张博涵), Daping He(何大平), and Shengxiang Wang(汪胜祥)
Chin. Phys. B, 2024, 33 (**3**): 037506. DOI: 10.1088/1674-1056/acfafa

Effect of TbF_3 diffusion on the demagnetization behavior and domain evolution of sintered Nd-Fe-B magnets by electrophoretic deposition

Xue-Jing Cao(曹学静), Shuai Guo(郭帅), Yu-Heng Xie(谢宇恒), Lei Jin(金磊), Guang-Fei Ding(丁广飞),Bo Zheng(郑波), Ren-Jie Chen(陈仁杰), and A-Ru Yan(闫阿儒)
Chin. Phys. B, 2023, 32 (**9**): 097503. DOI: 10.1088/1674-1056/acaf2d

Magnetic and electronic properties of bulk and two-dimensional $FeBi_2Te_4$: A first-principles study

Qianqian Wang(王倩倩), Jianzhou Zhao(赵建洲), Weikang Wu(吴维康), Yinning Zhou(周胤宁), Qile Li, Mark T. Edmonds, and Shengyuan A. Yang(杨声远)
Chin. Phys. B, 2023, 32 (**8**): 087506. DOI: 10.1088/1674-1056/acd522

Spin reorientation in easy-plane kagome ferromagnet $Li_9Cr_3(P_2O_7)_3(PO_4)_2$

Yuanhao Dong(董元浩), Ying Fu(付盈), Yixuan Liu(刘以轩), Zhanyang Hao(郝占阳), Le Wang(王乐), Cai Liu(刘才), Ke Deng(邓可), and Jiawei Mei(梅佳伟)
Chin. Phys. B, 2023, 32 (**5**): 057506. DOI: 10.1088/1674-1056/acc2b3

Magnetic and magnetocaloric effect of $Er_{20}Ho_{20}Dy_{20}Cu_{20}Ni_{20}$ high-entropy metallic glass

Shi-Lin Yu(于世霖)[1,†], Lu Tian(田路)[2,3], Jun-Feng Wang(王俊峰)[2,‡], Xin-Guo Zhao(赵新国)[1], Da Li(李达)[1], Zhao-Jun Mo(莫兆军)[2], and Bing Li(李昺)[1]

[1] *Shenyang National Laboratory for Materials Science, Institute of Metal Research, Chinese Academy of Sciences, Shenyang* 110016, *China and School of Materials Science and Engineering, University of Science and Technology of China, Shenyang* 110016, *China*

[2] *Ganjiang Innovation Academy, Chinese Academy of Sciences, Ganzhou* 341000, *China*

[3] *School of Materials Science and Engineering, Hebei University of Technology, Tianjin* 300130, *China*

(Received 22 November 2023; revised manuscript received 28 December 2023; accepted manuscript online 4 January 2024)

$Er_{20}Ho_{20}Dy_{20}Cu_{20}Ni_{20}$ high-entropy metallic glass exhibited excellent magnetic refrigeration material with a wide temperature range and high refrigeration capacity (RC) was reported. $Er_{20}Ho_{20}Dy_{20}Cu_{20}Ni_{20}$ high-entropy metallic glass was observed with typical spin glass behavior around 15.5 K. In addition, we find that the magnetic entropy change ($-\Delta S_M$) originates from the sample undergoing a ferromagnetic (FM) to paramagnetic (PM) transition around 20 K. Under a field change from 0 T to 7 T, the value of maximum magnetic entropy change ($-\Delta S_M^{max}$) reaches 12.5 J/kg·K, and the corresponding value of RC reaches 487.7 J/kg in the temperature range from 6 K to 60 K. The large RC and wide temperature range make the $Er_{20}Ho_{20}Dy_{20}Cu_{20}Ni_{20}$ high-entropy metallic glass be a promising material for application in magnetic refrigerators.

Keywords: magnetic materials, magnetocaloric effect, high-entropy metallic glass, magnetic refrigeration, large refrigeration capacity

PACS: 75.30.Sg, 75.47.Np **DOI:** 10.1088/1674-1056/ad1a94

1. Introduction

Nowadays, the energy conservation, emission reduction, and environmental protection have become development themes on a global scale.[1–5] The magnetocaloric effect (MCE) demonstrated by magnetic materials was considered as a promising alternative to conventional gas compression refrigeration for energy efficient refrigeration technology.[6–8] The MCE of magnetic refrigeration materials significantly determines the feasibility of this technology application. La(Fe, $Si)_{13}$-based compounds are considered as promising magnetic refrigeration materials for room temperature refrigeration and have received extensive attention and research, while there are still relatively fewer magnetic refrigeration candidates for the liquid hydrogen temperature region.[9–11] The Ericsson cycle is considered to be the optimal thermodynamic cycle for hydrogen liquefaction, which consists of two isothermal processes and two isomagnetic processes. Therefore, the development of magnetic refrigeration materials with table-like magnetic entropy changes for hydrogen liquefaction is essential.[12] In addition, cryogenic magnetic refrigeration technology is also increasingly receiving attention to potential applications in applications such as space science and hydrogen liquefaction. Hydrogen has been considered as one of the desirable clean energy sources because of its advantages such as high energy density and pollution free.[13] Therefore, it is imperative to develop magnetic refrigerants with remarkable performance around liquid hydrogen temperature (20 K).

In order to obtain magnetic refrigerants with wide temperature and high RC, researchers have made considerable attempts and efforts. Mo *et al.* found giant MCE in the polycrystalline compound TmGa because of two successive magnetic transitions.[14] Feng *et al.* reported amorphous/nanocrystalline composite fibers prepared by melt extraction method with a giant RC of 958 J/kg and a wide temperature range from 70 K to 270 K.[15] Furthermore, there is also searching for innovative approaches to design magnetic refrigeration materials with excellent MCE performance. High entropy (HE) alloys have received more attention in scientific research and engineering fields because of the properties of regulation, high corrosion resistance, high abrasive resistance, and high strength.[16–19] Meanwhile, metallic glasses (MGs) also demonstrates outstanding performance compared with crystalline materials, such as controllable Curie temperature, higher resistivity and broad $-\Delta S_M$ peak, which benefit the practical application in magnetic refrigeration systems.[20–22] The design of magnetic refrigeration materials with the advantages of HE MGs is gradually increasing as a topic of research. In addition, based on the De Gennes coefficient it is shown that the magnetic transition temperature decreases gradually as the RE atom increases from Gd–Tm.[23] Therefore, HE MGs with various rare earth elements are expected to achieve desirable magnetic refriger-

[†]Corresponding author. E-mail: slyu@imr.ac.cn
[‡]Corresponding author. E-mail: jfwang@gia.cas.cn

© 2024 Chinese Physical Society and IOP Publishing Ltd

ants with larger half-peak widths and high RCs compared to polycrystalline compounds. It has been demonstrated that ribbon magnetic refrigeration masses are more suitable for magnetic refrigeration systems than spherical shapes.[24] A series of HE MGs with wide temperature range and high RC have been reported, such as $Er_{20}Dy_{20}Co_{20}Al_{20}RE_{20}$ (RE = Gd, Dy, and Tm) $Ho_{20}Er_{20}Co_{20}Al_{20}RE_{20}$ (RE = Gd, Dy, and Tm), $Gd_{20}Ho_{20}Tm_{20}Cu_{20}Ni_{20}$.[25–27]

In this work, $Er_{20}Ho_{20}Dy_{20}Cu_{20}Ni_{20}$ HE MG was synthesized and the glass formation ability (GFA), magnetic, MCE were discussed. The $Er_{20}Ho_{20}Dy_{20}Cu_{20}Ni_{20}$ HE MG exhibits large RC in the temperature range from 6 K to 60 K. Our result shows that $Er_{20}Ho_{20}Dy_{20}Cu_{20}Ni_{20}$ HE MG is an ideal refrigerant for magnetic refrigerators.

2. Experiments

The elements Er, Ho, Dy, Cu, and Ni with a purity of 99.9 wt% were arc-smelted in an argon atmosphere. In order to reduce the sample loss, oxidation and ensure uniformity during the smelting process, Ti was used as an oxygen getter, and the melting was repeated four times with the lowest possible current. The ingots are then prepared into amorphous ribbons with thicknesses of 30 μm–40 μm and widths of 2 mm–3 mm after heating the ingots with an induction coil (surface velocity of 30 m/s) in a high-purity argon atmosphere. Bruker D8A A25 x-ray powder diffractometer (XRD, Cu $K\alpha$ radiation, 40 kV, 40 mA, $\lambda = 1.5418$ Å) was used to measure the structure of the amorphous ribbons. The HE MGs ribbons were used for the thermal analysis process and measured by differential scanning calorimeter (DSC) with a heating rate of 10 K/min. The magnetic data were measured on a quantum design physical property measurement system (PPMS-9) equipped with a superconducting quantum interference device (SQUID) and a vibrating sample magnetometer (VSM).

3. Results and discussion

The XRD pattern of the $Er_{20}Ho_{20}Dy_{20}Cu_{20}Ni_{20}$ HE MG at room temperature was shown in Fig. 1(a). It is not difficult to find a typical broad diffraction peaks and no obvious sharp crystalline peak. This indicates the formation of a completely glassy structure. In common with previously reported MGs materials, an endothermic reaction peak around the glass transition temperature can be observed on the DSC curve in Fig. 1(b).[24] The temperatures of T_g (glassy transition temperature), T_x (first crystallization), T_m (melting point), and T_l (liquidus temperature) marked with black arrows are 397 K, 513 K, 994 K, and 1040 K respectively for $Er_{20}Ho_{20}Dy_{20}Cu_{20}Ni_{20}$ HE MG. Consequently, the values of undercooled liquid region $\Delta T_x = (T_x - T_g)$ and the reduced glass transition temperature $T_{rg} = (T_g/T_l)$ indicators used to evaluate the performance of glass formation are 116 K and 0.38, respectively. A supercooled liquid region of up to 116 K and a lower T_{rg} are obtained due to the mixing of multiple elements and the large atomic radius difference between Cu and Ni elements with rare earth elements, which indicates the high thermal stability of the MG with respect to crystallisation.

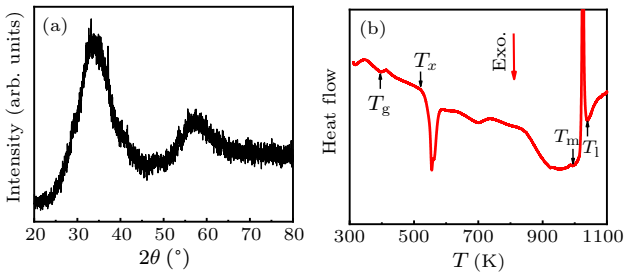


Fig. 1. (a) The XRD patterns of $Er_{20}Ho_{20}Dy_{20}Cu_{20}Ni_{20}$ HE MG at roomtemperature. (b) The DSC curves were measured at a rate of 10 K/min.

The zero-field cooling (ZFC) and field cooling (FC) modes of $Er_{20}Ho_{20}Dy_{20}Cu_{20}Ni_{20}$ HE MG under a magnetic field (H) of 0.01 T were shown in Fig. 2. It is not difficult to find that there exists an obvious spin freeze transition process with a sharp peak in the ZFC curve and a large bifurcation between the ZFC and FC curves, which is typical of spin glass (SG) behavior.[28] The magnetic transition temperature was determined from the inflection point in the dM/dT curve as shown in the illustration in Fig. 2. The inflection point at 15.5 K was the spin freezing temperatures (T_f) associated with a metastable state of spin glass to the ferromagnetic (FM) state, and with increasing temperature, another abrupt change at 20 K corresponded to a magnetic transition from FM to paramagnetic (PM) state.

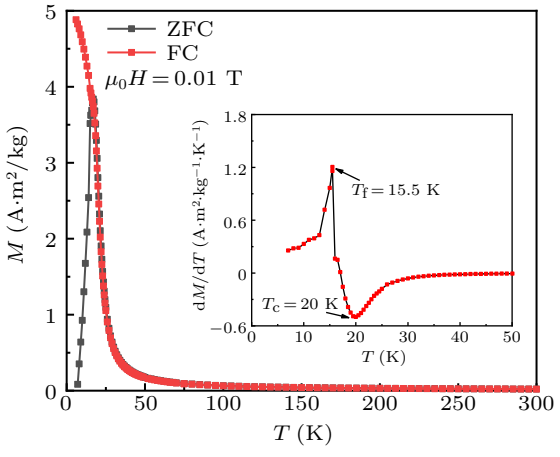


Fig. 2. The temperature dependence of the magnetic susceptibility of ZFC and FC at 0.01 T, the inset is a schematic diagram of the dM/d–T curve.

The temperature dependence of the inverse magnetic susceptibility $1/\chi$ (T) of ZFC was shown in Fig. 3(a). It is obvious that the inverse molar susceptibility is linear and fit to the Curie–Weiss law $1/\chi = (T - \theta_p)$. The PM Curie temperature θ_p of 11.42 K indicates FM state for $Er_{20}Ho_{20}Dy_{20}Cu_{20}Ni_{20}$

HE MG. The experimental value of the effective magnetic moment obtained from the Curie–Weiss fitting is 9.5 μ_B, which is close to the theoretical magnetic moments of Er^{3+} (9.5 μ_B), Ho^{3+} (10.6 μ_B), Dy^{3+} (10.60 μ_B) free ion. The magnetization *versus* temperature dependence under different magnetic fields was illustrated in Fig. 3(b). The non-zero orbital angular momentum in the rare-earth ions Er, Ho, Dy results in large random magnetic anisotropy, which breaks the long-range ferromagnetic order. In the low-temperature region the spin is strongly oriented along the anisotropy axis, leading to the formation of SG states with random magnetic moment orientation and magnetic irreversibility. It was obviously shown that the orientation along the anisotropic axis gradually converges with increasing magnetic field (0.4 T) in Fig. 3(b). This typical spin glass behavior is also observed in $Er_{20}Dy_{20}Co_{20}Al_{20}Gd_{20}$ HE MG.

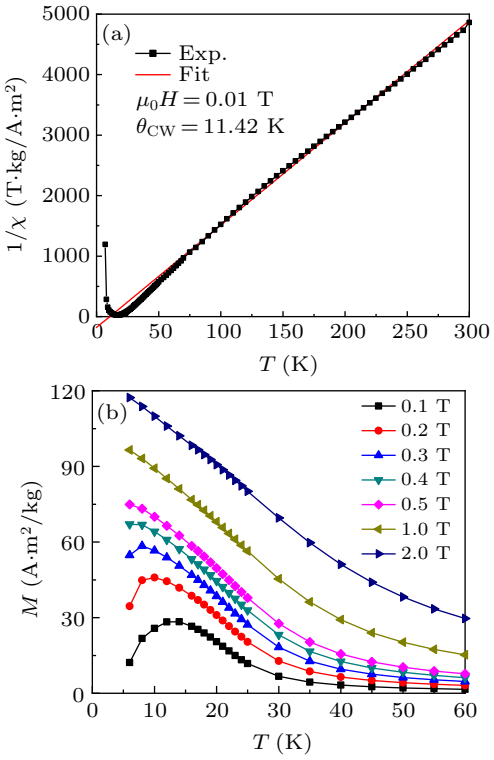


Fig. 3. (a) ZFC inverse molar susceptibility $1/\chi$ fitted to the Curie–Weiss law for $Er_{20}Ho_{20}Dy_{20}Cu_{20}Ni_{20}$ HE MG. (b) Temperature dependence of magnetization for $Er_{20}Ho_{20}Dy_{20}Cu_{20}Ni_{20}$ HE MG under various magnetic fields.

The isothermal magnetization (M–H) curves of $Er_{20}Ho_{20}Dy_{20}Cu_{20}Ni_{20}$ HE MG at magnetic fields up to 7 T are shown in Figs. 4(a) and 4(b). The magnetization of the studied glass alloy increases dramatically at temperatures below T_c, which was clearly characteristic of the ferromagnetic state. The magnetization curve gradually flattens out as the temperature rises near T_c, indicating that the magnetic structure changes from FM to PM. The magnetization isotherms below T_c under low magnetic field were shown in Fig. 4(b). The intersection of the magnetization curves below 18 K was attributed to the magnetic behavior of the spin glasses, and a similar phenomenon was observed in $Er_{20}Dy_{20}Co_{20}Al_{20}Gd_{20}$ HE MG and GdNiAl alloys.[24,29]

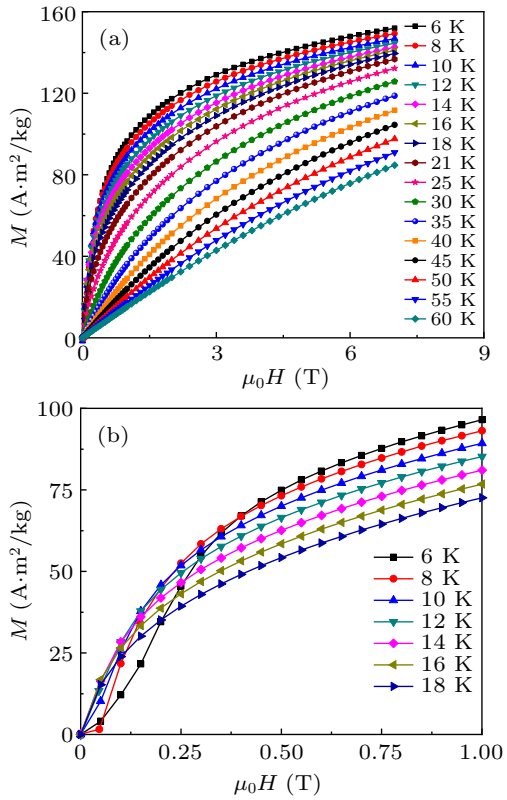


Fig. 4. (a) Isothermal magnetization curve of $Er_{20}Ho_{20}Dy_{20}Cu_{20}Ni_{20}$ HE MG. (b) Isotherms magnetization curve of $Er_{20}Ho_{20}Dy_{20}Cu_{20}Ni_{20}$ HE MG at 6 K–18 K ($\Delta T = 2$ K), respectively.

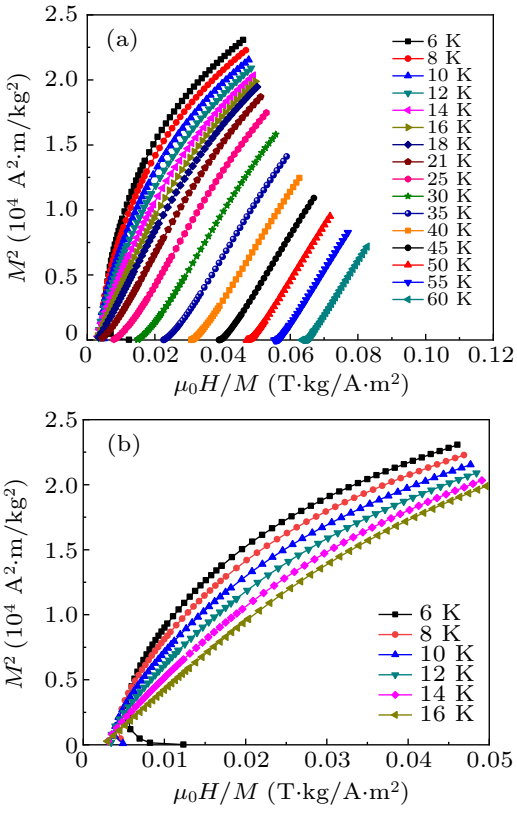


Fig. 5. (a) The Arrott plots for the $Er_{20}Ho_{20}Dy_{20}Cu_{20}Ni_{20}$ HE MG. (b) The illustrations show the enlarged diagrams of Arrott at 6 K, 8 K, 10 K, 12 K, and 14 K, respectively.

To better comprehend the magnetic performance of $Er_{20}Ho_{20}Dy_{20}Cu_{20}Ni_{20}$ HE MG, the Arrott curves (M^2 *versus* H/M) were measured at different temperatures and the corresponding results are shown in Fig. 5(a). According to the Banerjee criterion the magnetic phase transition is of the second order type for all slopes of the Arrott diagram to be positive, and when the slope is negative, it corresponds to the first order type of magnetic phase transition.[30] It is remarkable that the S-shaped curve exists at temperatures below T_f (< 15.5 K) with a significant negative slope, and the inflection point corresponding to H/M gradually decreases with increasing temperature, the corresponding result was demonstrated in Fig. 5(b), which was attributable to the spin-glass behavior. In addition, positive slopes are observed at temperatures above T_f, indicating the presence of a second order magnetic transition in the $Er_{20}Ho_{20}Dy_{20}Cu_{20}Ni_{20}$ HE MG.

The value of $-\Delta S_M$ is an important indicator of the performance of the magnetocaloric effect. Define $-\Delta S_M$ by integrating the Maxwell's relation for the magnetic field:

$$\begin{aligned}\Delta S(T,H) &= S_M(T,H) - S_M(T,0) \\ &= \int_{H_0}^{H_{max}} \left(\frac{\partial M}{\partial H}\right) dH, \end{aligned} \tag{1}$$

where H_{max} and H_0 indicates the maximum and minimum values of the magnetic fields. The $-\Delta S_M$ was calculated from the isothermal magnetization measurement results *versus* temperature at various magnetic fields as shown in Fig. 6.

It needs to be emphasized that $-\Delta S_M^{max}$ was observed near T_c, which was attributable to the transition from FM to PM, while the $-\Delta S_M$ anomaly near T_f was associated with the spin glass to the FM state. It implies that the $-\Delta S_M$ originates mainly from the second-order magnetic phase transition from ferromagnetic to paramagnetic, while the spin-glass behavior at low temperatures contributes only a small part of $-\Delta S_M$. The value of $-\Delta S_M^{max}$ were 4.4 J/kg·K, 9.8 J/kg·K, and 12.5 J/kg·K around T_c under varying magnetic fields of 0–2 T, 0–5 T, and 0–7 T, respectively. It is remarkable that the peak of the $-\Delta S_M^{max}$ gradually shifted to higher temperatures with increasing magnetic field reflecting the typically characteristic features of FM, which is consistent with the results obtained above. The RC is the volume of heat that a magnetic refrigeration material is able to transfer from the cold sink to the exothermic sink of the refrigerant in a refrigeration cycle, and is another important parameter to measure the magnetocaloric effect. The RC values of the $Er_{20}Ho_{20}Dy_{20}Cu_{20}Ni_{20}$ HE MG were evaluated based on the relations proposed by Gschneidner *et al.*[31]

$$RC = \int_{T_1}^{T_2} |\Delta S_M| \, dT, \tag{2}$$

where T_1 and T_2 in the relation are the corresponding temperatures on each side of half of $-\Delta S_M^{max}$, respectively.

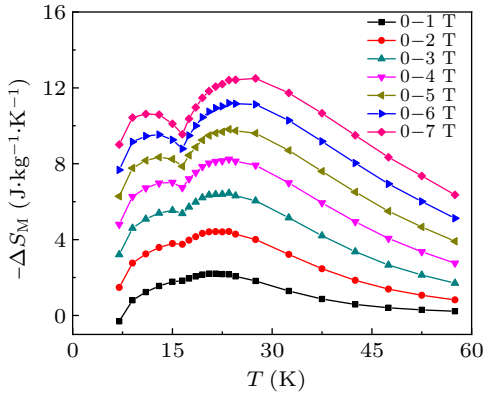


Fig. 6. The magnetic entropy change $-\Delta S_M$ of the $Er_{20}Ho_{20}Dy_{20}Cu_{20}Ni_{20}$ HE MG as a function of temperature under applied magnetic fields of 0 T–7 T.

The values of RC for $Er_{20}Ho_{20}Dy_{20}Cu_{20}Ni_{20}$ HE MG are 106 J/kg, 330.5 J/kg, and 487.7 J/kg under varying magnetic fields of 0–2 T, 0–5 T, and 0–7 T, respectively. The MCE of some recently reported magnetic refrigeration compounds with magnetic phase transition temperatures comparable to $Er_{20}Ho_{20}Dy_{20}Cu_{20}Ni_{20}$ HE MG was shown in Table 1. The $Er_{20}Ho_{20}Dy_{20}Cu_{20}Ni_{20}$ HE MG has a wide temperature range and high RC, which is beneficial to the practical application of the magnetic refrigeration systems. Consequently, our work provides an attractive refrigerant for magnetic refrigerators with wide application potential in the field of the hydrogen liquefaction.

Table 1. Comparative magnetocaloric properties of $Er_{20}Ho_{20}Dy_{20}Cu_{20}Ni_{20}$ HE MG and other magnetic refrigeration materials in the region of similar magnetic phase transitions.

Compounds	T_M (K)	$-\Delta S_M^{max}$ (J·kg^{-1}·K^{-1})		RC (J·kg^{-1})	References
		0–2 T	0–5 T	0–5 T	
$Er_{20}Ho_{20}Dy_{20}Cu_{20}Ni_{20}$ MGs	20	4.4	9.8	330.7	this work
$Dy_{50}Gd_7Al_{23}Co_{20}$ MGs	26	4.33	9.77	290	[32]
ErZn/$ErZn_2$ composite	9/20	8.1	19.5	365	[33]
$Ho_{20}Er_{20}Co_{20}Al_{20}Tm_{20}$ MGs	9	–	15	375	[26]
$Er_{0.2}Tm_{0.2}Ho_{0.2}Cu_{0.2}Co_{0.2}$ MGs	13.5	–	15.7	448.1	[34]
$Dy_{36}Ho_{20}Co_{20}Al_{24}$ MGs	18	–	12.6	468	[34]

4. Conclusions

In conclusion, $Er_{20}Ho_{20}Dy_{20}Cu_{20}Ni_{20}$ HE MG was successfully synthesized and GFA, magnetic properties, MCE were researched. The $-\Delta S_M$ originates from the second-order phase transition from FM to PM around 20 K. Below T_c, a noticeable spin-glass behavior was observed. The $-\Delta S_M^{max}$ and RC are 12.5 J/kg·K and 487.7 J/kg under varying the magnetic field from 0–7 T, respectively. The outstanding MCE properties make $Er_{20}Ho_{20}Dy_{20}Cu_{20}Ni_{20}$ HE MG a promising candidate refrigerant in the hydrogen liquefaction temperature range. Meanwhile, the method of designing HE MG magnetic refrigeration material by doping with various rare earth elements provides a useful method to obtain refrigeration materials with large temperature range. More importantly, the research on $Er_{20}Ho_{20}Dy_{20}Cu_{20}Ni_{20}$ HE MG has provided additional ideas for understanding the magnetic behaviors of MG.

Acknowledgements

Project supported by the National Natural Science Foundation of China (Grant Nos. 52371203 and 52271192) and the Ministry of Science and Technology of China (Grant No. 2021YFB3501201).

References

[1] Li L W and Yan M 2023 *J. Mater. Sci. Technol.* **136** 1
[2] Zhang Y K, Tian Y, Zhang Z Q, Jia Y S, Zhang B, Jiang M Q, Wang J and Ren Z M 2022 *Acta Mater.* **226** 117669
[3] Yang S X, Zheng X Q, Wang D S, Xu J P, Yin W, Xi L, Liu C F, Liu J, Xu J W, Zhang H, Xu Z Y, Wang L C, Yao Y H, Zhang M S, Zhang Y C, Shen J X, Wang S G and Shen B G 2023 *J. Mater. Sci. Technol.* **146** 168
[4] Ma Z P, Xu P, Ying J Y, Zhang Y K and Li L W 2023 *Acta Mater.* **247** 118757
[5] Mo Z J, Gong J J, Xie H C, Zhang L, Fu Q, Gao X Q, Li Z X and Shen J 2023 *Chin. Phys. B* **32** 027503
[6] Zhang Y, Shi G Y, Wang L C, Zheng X Q, Liu J, Jin Y X, Zhang K W, Liu H X, Zong S T and Sun Z G 2022 *Chin. Phys. B* **31** 077501
[7] Zhang Y K, Hao W X, Hu C L, Wang X, Zhang X F and Li L W 2023 *Adv. Funct. Mater.* **33** 2310047
[8] Zhang Y K, Xu P, Zhu J, Yan S M, Zhang J C and Li L W 2023 *Mater. Today Phys.* **32** 101031
[9] Doring A M, Rosa M A, Hemkemaier M C, Wendhausen P A P, Lozano J A, Barbosa J R and Teixeira C D 2022 *J. Alloys Compd.* **902** 163688
[10] Zhong X C, Dong X T, Huang J H, Liu C L, Zhang H, Huang Y L, Yu H Y and Ramanujan R V 2022 *Metals* **121** 112
[11] Law J Y, Diaz-Garcia A, Moreno-Ramirez L M and Franco V 2021 *Acta Mater.* **212** 116931
[12] Li L W, Oliver N, Marcel K and Rainer P 2014 *Appl. Phys. Lett.* **104** 092416
[13] Tarhan C and Cil M A 2021 *J. Energy. Storage* **40** 102676
[14] Mo Z J, Shen J, Yan L Q, Tang C C, Lin J, Wu J F, Sun J R, Wang L C, Zheng X Q and Shen B G 2013 *Appl. Phys. Lett.* **103** 052409
[15] Feng J Q, Liu Y H, Sui J H, He A N, Xia W X, Wang W H, Wang J Q and Huo J T 2021 *Mater. Today. Phys.* **21** 100528
[16] Yeh J W, Chen S K, Lin S J, Gan J Y, Chin T S, Shun T T, Tsau C H and Chang S Y 2004 *Adv. Eng. Mater.* **6** 299
[17] Singh S, Wanderka N, Murty S, Glatzel U and Banhart J 2010 *Acta Mater.* **59** 182
[18] He J Y, Zhu C, Zhuo D Q, Liu W H, Nieh T G and Lu Z P 2014 *Intermetallics* **55** 9
[19] Zhang Y, Zou T T, Tang Z, Michael G, Karin A D, Peter K L and Lu Z P 2014 *Prog. Mater. Sci.* **61** 1
[20] Zhao S F, Shao Y, Liu X, Chen N, Ding H Y and Yao K F 2015 *Mater. Des.* **87** 625
[21] Tian L, Xu B, Chen H, Mo Z J, Li Z X, Liu G D and Shen J 2023 *Sci. China Mater.* **66** 3984
[22] Luo Q A, Schwarz B, Mattern N and Eckert J 2010 *Phys. Rev. B* **82** 024204
[23] Smaili A and Chahine R 1997 *J. Appl. Phys.* **81** 824
[24] Vuarnoz D and Kawanami T 2012 *Appl. Therm. Eng.* **37** 388
[25] Li J, Xue L, Yang W M, Yuan C C, Huo J T and Shen B L 2018 *Intermetallics* **96** 90
[26] Huo J T, Huo L S, Li J W, Men H, Wang X M, Inoue A, Chang C T, Wang J Q and Li R W 2015 *J. Appl. Phys* **117** 073902
[27] Zhang Y K, Wu B B, Guo D, Wang J and Ren Z M 2021 *Chin. Phys. B* **30** 017501
[28] Zhang Y K, Guo D, Li H D, Geng S H, Wang J, Li X, Xu H, Ren Z M and Wilde G 2018 *J. Alloys Compd.* **733** 40
[29] Yuan F, Du J and Shen B L 2012 *Appl. Phys. Lett.* **101** 032405
[30] Fan J F, Ling L S, Hong B, Zhang L, Pi L and Zhang Y H 2010 *Phys. Rev. B* **81** 144426
[31] Luo Q, Zhao D Q, Pan M X and Wang W H 2007 *Appl. Phys. Lett.* **90** 211903
[32] Li L W, Yuan Y, Qi Y, Wang Q and Zhou S Q 2018 *Mater. Res. Lett.* **6** 67
[33] Dong Z Q, Wang Z J and Yin S H 2020 *Intermetallics* **124** 106879
[34] Liang L, Hui X, Zhang C M and Chen G L 2008 *J. Alloys Compd.* **463** 30